ACS APPLIED MATERIALS & INTERFACES

Research Article

www.acsami.org

# Fabrication and Properties of a Branched $(NH_4)_xWO_3$ Nanowire Array Film and a Porous $WO_3$ Nanorod Array Film

Ya Liu,[†] Liang Zhao,[†] Jinzhan Su,[†] Mingtao Li,*[,†] and Liejin Guo[†,‡]

[†]International Research Center for Renewable Energy, State Key Laboratory of Multiphase Flow in Power Engineering, Xi'an Jiaotong University, Shaanxi 710049, China

[‡]The College of Engineering, Department of Mechanical Thermal Engineering and Chemical & Material Engineering, King Abdulaziz University, Jeddah 21589, Saudi Arabia

Ⓢ *Supporting Information*

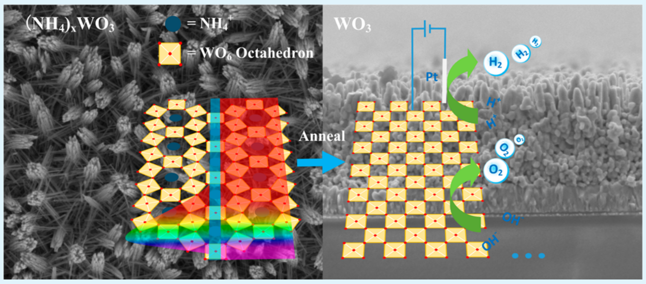

**ABSTRACT:** We describe the successful fabrication of a three-dimensional branched $(NH_4)_xWO_3$ nanowire array film on fluorine-doped tin oxide coated glass by a facile one-step hydrothermal method. The porous $WO_3$ nanorod array film formed after heat treatment and recrystallization. Specifically, the branched $(NH_4)_xWO_3$ nanowire array film has very thin nanowires that were about 10 nm in diameter. The results of an optical and photoelectrochemical test show that the branched $(NH_4)_xWO_3$ nanowire array film could be used as a near-infrared shielder, while the porous $WO_3$ nanorod array film can be used as a photoanode for water splitting. Moreover, the morphology, structure, and composition of the as-prepared films are revealed, and the related changes caused by heat treatment are discussed in detail.

**KEYWORDS:** *branched, film, porous, tungsten, water splitting*

## INTRODUCTION

Three-dimensional (3D) branched nanostructures have attracted much attention because of the unique characteristics that include large specific surface, hierarchy structure, excellent light-trapping characteristics, and direct electron-transport pathways.[1,2] Particularly, 3D branched nanostructures exert more influence in many nanoscale device applications.[3,4] For example, a photoanode with branched nanostructure has photocatalytic abilities superior to those of bare nanorods without branches, owing to the large contact area with the electrolyte and excellent light-trapping characteristics.[5] Furthermore, the branched $\alpha$-$Fe_2O_3/SnO_2$ composite anode material exhibited relatively low initial irreversible loss and high reversible capacity when used for lithium-ion batteries.[6] Additionally, a asymmetric supercapacitor based on 3D hierarchical $MnMoO_4/CoMoO_4$ heterostructured nanowires that could improve the electrochemical properties has been demonstrated.[7]

So far, various materials and techniques have been demonstrated to form 3D branched nanostructures.[8−14] To the best of our knowledge, there are few articles on the fabrication of branched tungsten bronze compounds ($M_xWO_3$). Most $M_xWO_3$ compounds were formed in nanoparticles or one-dimensional (1D) nanostructures.[15−25] Among them, some $M_xWO_3$ (M = Cs, K, and $NH_4$) powders were prepared by liquid deposition and exhibited excellent near-infrared (NIR) shield properties.[15−20] Moreover, hydrogen tungsten bronze ($H_xWO_3$) could be used as the electrocatalyst[21] or decoking agent for solid oxide fuel cells.[22] Besides, $(NH_4)_xWO_3$ and $H_xWO_3$ with special nanostructures could also serve as intermediates for the fabrication of $WO_3$ nanostructures.[23−25] Because of superior photocatalytic, electrochromic, and electrocatalytic properties, $WO_3$-based photoelectrodes are used extensively.[26−39] Thus, if branched tungsten bronze compounds were employed in these areas, the performance may be better.

In this article, we present a facile one-step hydrothermal process for the fabrication of a 3D branched $(NH_4)_xWO_3$ nanowire array film. The purpose of this study is to discuss the morphology, structure, and composition of this novel 3D branched nanowire array film and reveal the related changes during heat treatment. In addition, the optical and photoelectrochemical (PEC) properties of the films were investigated to provide reference material for potential applications.

## EXPERIMENTAL SECTION

**Film Synthesis.** Before deposition, the substrate, fluorine-doped tin oxide (FTO)-coated glass, was cleaned in acetone, deionized water, and ethanol ultrasonically and then dried with a stream of nitrogen. An ammonium wolframate ($H_{40}N_{10}O_{41}W_{12}\cdot xH_2O$) solution in lactic acid was heated for dissolution, and the concentration was controlled at 10 wt %. Then, the seed layer precursor solution was prepared by diluting

**Received:** October 19, 2014
**Accepted:** January 27, 2015
**Published:** January 27, 2015

DOI: 10.1021/am507230t
*ACS Appl. Mater. Interfaces* 2015, 7, 3532−3538

the ammonium wolframate solution 10 times by volume with ethanol. Subsequently, the precursor solution was deposited on the substrate via a spin-coating process. The coated substrate was annealed at 500 °C for 3 h in a muffle furnace to form the $WO_3$ seed layer.

The hydrothermal precursor solution was prepared by mixing 1.25 g of an ammonium wolframate solution (10 wt %) with 8.75 g of lactic acid, 20 g of ethanol, and 0.1383 g of L-glutathione reduced ($C_{10}H_{17}N_3O_6S$). This solution and the seed-layer-coated substrate were placed within a Teflon-lined stainless steel autoclave and then maintained at 200 °C for 4 h. After the synthesis process, the resulting film, a branched $(NH_4)_xWO_3$ nanowire array film, was cleaned with ethanol. Furthermore, the porous $WO_3$ nanorod array photoanode can be achieved by annealing the as-prepared branched $(NH_4)_xWO_3$ nanowire array films in air at 350 or 550 °C for 1 h, while the temperature rise rate was kept at 25 °C/min.

**Characterization.** The surface chemical components and states of the films were determined by X-ray photoelectron spectroscopy (XPS) measurements, which were conducted by using a Kratos spectrometer (Axis Ultra$^{DLD}$) with monochromatic Al K$\alpha$ radiation ($h\nu$ = 1486.69 eV). The binding energies were calibrated against the C 1s signal (adventitious carbon), which was centered at 284.8 eV. X-ray diffraction (XRD) analysis was conducted on an X'pert PRO diffractometer [PANalytical, using Cu Ka irradiation ($\lambda$ = 15.4184 nm)]. The morphology and structure were characterized using transmission electron microscopy (TEM; FEI Tecnai G2 F30) and scanning electron microscopy (SEM; JEOL JSM-7800F). Thermogravimetric (TG) analysis was performed with a STA 449C thermal analyzer from NETZSCH. The optical properties were analyzed by a double-beam UV4100 UV−vis−NIR spectrophotometer.

**PEC Measurement.** The PEC measurements were carried out in a three-electrode system. The sample, a platinum foil, and a saturated calomel electrode (SCE) were used as the work, counter, and reference electrodes, respectively. A 0.5 M $Na_2SO_4$ solution in water was used as the electrolyte. A 500 W xenon lamp coupled with an AM1.5 filter was used as the light source, and the light intensity was set at 100 mW/cm$^2$. The photocurrent densities were measured by a CHI 760D scanning potentiostat (CH Instruments).

## ■ RESULTS AND DISCUSSION

After a hydrothermal process, a blue transparent film was achieved on a FTO-coated substrate. It can be seen in the Experimental Section that all elements in the precursor solution are W, O, C, N, H, and S. XPS was used to further characterize the chemical composition of the as-prepared film. However, O, C, and H cannot be determined accurately by XPS because O and C may come from the atmosphere and XPS is sensitive to all elements except H and He. The survey-scan XPS spectrum is shown in Figure 1 and indicates that the elements W and N certainly exist in the film. Moreover, no peak of S can be found, which demonstrates the inexistence of element S. Thus, from the survey-scan XPS spectrum results, we can infer that the elements W and N certainly exist, while the elements O, C, and H are potential candidates.

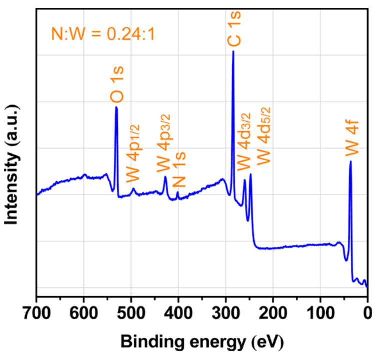

**Figure 1.** Survey-scan XPS spectrum of the branched $(NH_4)_xWO_3$ nanowire array film.

Figure 2a displays the XRD pattern of the blue transparent film. On the basis of elemental analysis of XPS, all peaks were indexed to standard card JCPDS 42-1286, which corresponds to hexagonal $(NH_4)_{0.33}WO_3$, and no any other characteristic peak for impurity $WO_3$ or $WO_{3-x}$ exists. However, the quantitative analysis of surfaces (Figure 1) shows that the ratio of atomics N/W is 0.24. The ratio of atomics N/W for $(NH_4)_{0.33}WO_3$ does not match the result of XPS for the blue transparent film. Is the formula of the as-prepared sample $(NH_4)_{0.33}WO_3$ (based on the current analysis), or is something wrong? Previous works show that this "noncorrespondence" was due to a rigid W−O framework existing in hexagonal ammonium tungsten bronze.[15,40,41] The framework is built of layers that are made of the corner-sharing $WO_6$ octahedra, and the layers are stacked along the *c* axis, as shown in Figure 2b. Because the $WO_6$ octahedra are arranged in six-membered rings, the superposition of vacancies in the corner-sharing $WO_6$ octahedra leads to 1D hexagonal channels randomly occupied by ammonia ions and creates an uncertainty of "$x$" in $(NH_4)_xWO_3$. Hence, the formula of the as-prepared blue transparent film is $(NH_4)_xWO_3$.

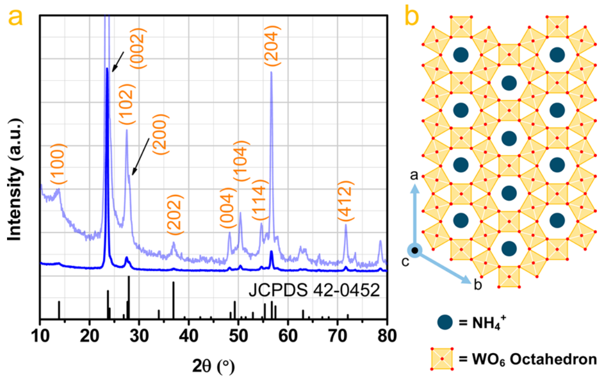

**Figure 2.** (a) XRD pattern of the branched $(NH_4)_xWO_3$ nanowire array film. The dark-blue line represents the complete pattern, while the light-blue line represents an amplified pattern along the vertical axis. (b) Projection on the *ab* plane of the hexagonal $M_xWO_3$ framework.

The surface morphology of the $(NH_4)_xWO_3$ film is shown in Figure 3a−c from different perspectives. The uniform and densely branched nanowires grew regularly on the FTO layer like a "forest". The thickness of the film was about 1.5 $\mu$m. Each trunk was made up of a bunch of nanowires. The diameter of the branch looks extremely small. Of note is that the branches preferred to grow along the diagonal directions of the hexagonal prism in nature, as shown in the enlarged SEM photographs (Figure 3c).

The TEM and HRTEM images depicted in Figure 2d−g provide a clear presentation of the growth direction of the trunks and branches. In the direction parallel to both the trunks and branches, the distance of the planes was calculated as 0.378 nm, which was consistent with the interplanar spacing of the (002) planes, confirming that both trunks and branches grew along the *c* axis. Meanwhile, the XRD pattern in Figure 2a also shows that the peak area of the (002) planes was extremely higher than the other peaks, also suggesting the preferential growth of nanowires along the *c* axis. Both results can be

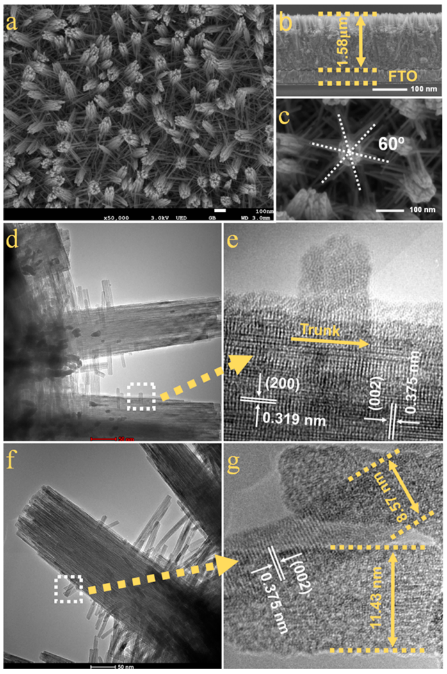

**Figure 3.** (a−c) SEM, (d and f) TEM, and (e and g) HRTEM images of the branched $(NH_4)_xWO_3$ nanowire array film.

confirmed mutually. Moreover, the TEM image shows that the diameter of the branches was around 10 nm.

To study the branched nanowire growth process, SEM images were taken for the films with different preparation conditions, as shown in Figures S1 and S2 in the Supporting Information (SI). Figure S1 in the SI shows morphologies of FTO, the seed layer, and the branched $(NH_4)_xWO_3$ nanowire array film without the seed layer or glutathione. Before hydrothermal treatment, the $WO_3$ nanoparticles in the seed layer were difficult to recognize (Figure S1b in the SI). However, Figure S1c in the SI indicates that the absence of the seed layer can lead to conglobation of the branched nanowires. Thus, we can conclude that the seed layer really did exist and had a significant influence on the crystal growth. Moreover, Figure S1d in the SI shows that the branched structure still formed without glutathione. Thus, the branched structure was not caused by glutathione. Previous works showed that the biomolecules of glutathione could be used as capping agents by being adsorbed onto some specific crystal planes.[42,43] In this work, glutathione significantly inhibited the growth of the (100) planes and, hence, contributed to the thin branch, the unevenness top, and the large surface area. Figure S2 in the SI shows the SEM images of the branched $(NH_4)_xWO_3$ nanowire array film for different growth periods. At the beginning of the growth period, the branch started to grow as soon as the trunk grew. As time went on, the trunk grew in length, while the original branch (close to the FTO substrate) stopped growing because of limited space. This is the reason why the surface of the film presents a forestlike structure and the bottom of the film presents a more dense structure. Additionally, the inset SEM image at low magnification in Figure S2c in the SI indicates that an excessively long hydrothermal time could make the film fall off easily from FTO.

On the basis of the above analysis, the schematic illustration of the growth of the branched $(NH_4)_xWO_3$ nanowire array film is displayed in Figure 4. In particularly, as both trunks and branches grew along the *c* axis, it is reasonable to expect that there should be a "transition point" that joined the (001) and (100) crystal planes together. Although it is difficult to clearly show this "transition point" by means of instrument measurement, we believe lactic acid might dominate the formation of this "transition point" by promoting the formation of crystals on the (100) crystal plane. Therefore, branches grew in all six directions that denote the family of {100} planes.

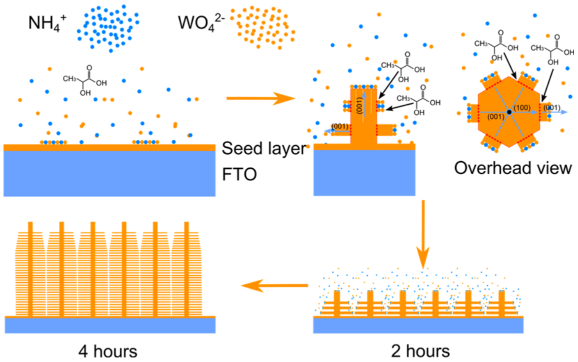

**Figure 4.** Schematic illustration of the growth of the branched $(NH_4)_xWO_3$ nanowire array film.

As mentioned above, "*x*" is a variable in $(NH_4)_xWO_3$. To study the related changes of the morphology, structure, and composition of this novel branched $(NH_4)_xWO_3$ nanowire array film during heat treatment, TG analysis was investigated in an air atmosphere. Figure 5 displays the TG plot. The heating rate was 10 °C/min. According to the plot, an initial weight loss was found up to around 252 °C, which may be ascribed to the departure of surface-absorbed water and structural water elimination,[15,16] while the weight loss in the temperature range of 252−515 °C may be attributed to the release of $NH_3$ from $(NH_4)_xWO_3$.[15] However, a gradual weight increase was detected in the temperature range of 515−700 °C. The extra weight ought to come from the air atmosphere and may be caused by residual oxygen deficiency.[15,16] As shown in the previous works, the removal of residual oxygen deficiency can be expressed as $WO_{3-x} \rightarrow WO_3$ and thus increase the oxygen content in the film while the tungsten content remains constant.[15,16]

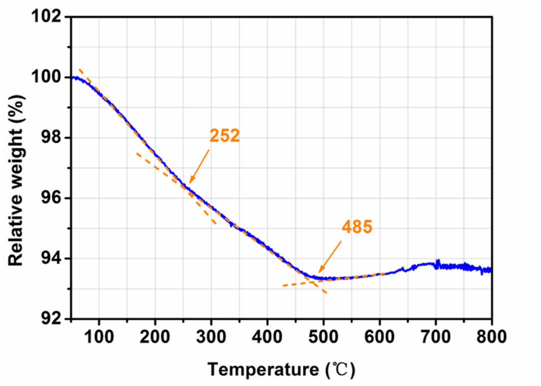

**Figure 5.** TG plot of the branched $(NH_4)_xWO_3$ nanowire array film recorded in air.

To be clear about the changes revealed in the TG plot, two branched $(NH_4)_xWO_3$ nanowire array films were annealed with a muffle furnace in an air atmosphere at temperatures of 350 and 550 °C for 2 h. The annealed temperature was selected in the middle of two transformation sections (252−515 and 515−700 °C). Figure 6 shows the XRD patterns of the branched $(NH_4)_xWO_3$ nanowire array and the two annealed films. After annealing at 350 °C, theres appeared to be a slight but obvious shift to the lower angle in the character peaks. On the basis of the previous analysis, this shift was caused by the release of $NH_3$. Meanwhile, this shift also indicates an increase of the lattice parameter. When the annealed temperature was 550 °C, some new peaks appeared. All of these new peaks were indexed to standard card JCPDS 43-1035, indicating the formation of monoclinic $WO_3$, while no other secondary $WO_3$ phase existed. The results of XRD analysis are consistent with those of the TG plot.

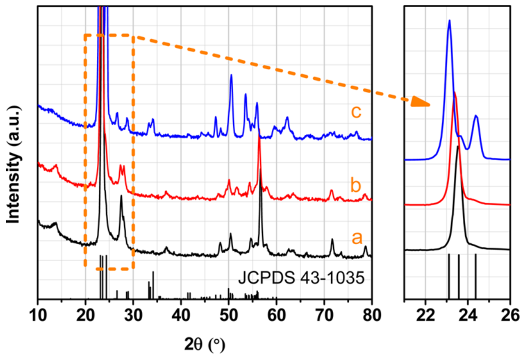

**Figure 6.** XRD patterns and digital photographs of (a) the branched $(NH_4)_xWO_3$ nanowire array film, (b) the 350 °C annealed film, and (c) the 550 °C annealed film.

The valence states of the elements W and N in the films were performed by high-resolution XPS, as shown in Figure 7. During deconvolution of the W 4f levels, the full width at half-maximum ratios of the $4f_{5/2}$ to $4f_{7/2}$ levels were fixed at 1.0, and the spin−orbit splitting of the doublet was 2.1 eV (with an area ratio of 4:3).[18,19,40,45] The ratio of atomics N/W changes from 0.24 to 0.073 to 0 as the annealing temperature increases, confirming the release of $NH_3$. For the unannealed film and the 350 °C annealed film, two pairs of W 4f peaks exist that index to $W^{6+}$ and $W^{5+}$ separately. The peaks of $W^{5+}$ indicate the existence of oxygen deficiency, and low-temperature annealing cannot remove the oxygen deficiency entirely. Therefore, residual oxygen deficiency existing in the film led to a weight increase in the temperature range of 515−700 °C during TG analysis. Moreover, the binding energy of $W^{6+}$ expresses an obvious shift to low energy. Because the binding energy can intuitively reflect the circumstances of the atom, this shift, we believe, should be contributed by the combined effect of a larger lattice parameter, the release of $NH_3$, and the disappearance of oxygen deficiency. The schematic illustration of lattice evolution is illustrated in Figure 7.

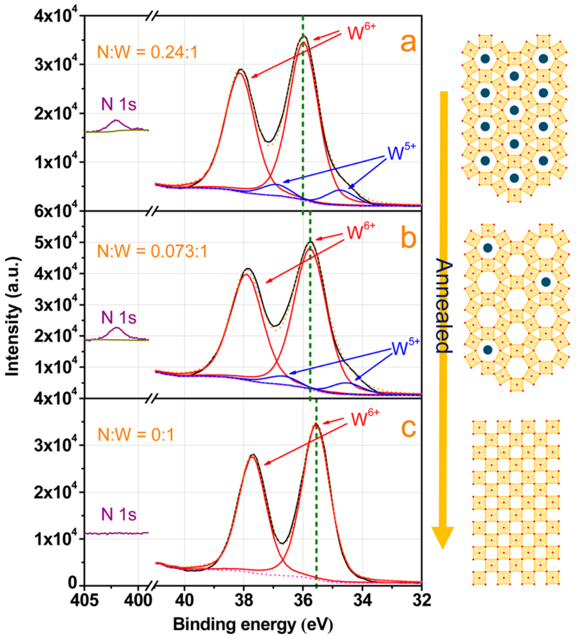

**Figure 7.** High-resolution XPS spectra of N 1s and W 4f and schematic illustrations of lattice evolution for (a) the branched $(NH_4)_xWO_3$ nanowire array film, (b) the 350 °C annealed film, and (c) the 550 °C annealed film.

Figure 8 shows the SEM images of the two annealed films. There is no significant difference in the unannealed film and the 350 °C annealed film. However, the 550 °C annealed film has a porous structure, while the branched nanowire array disappears and transforms into vague 1D nanorods. Moreover, on the surface of the 550 °C annealed film, many nanosteps (pointed out by the arrows) can be observed clearly. This may be caused by the crystal slip at the interface between the layers during recrystallization. So far, the related changes of the morphology, structure, and composition during heat treatment are clear. To provide a more detailed review, Figures S3 and S4 in the SI display the XRD patterns and high-resolution XPS spectra of 250 and 450 °C annealed films, and the results well reconfirmed the conclusions about the crystallization process and chemical changes upon calcination.

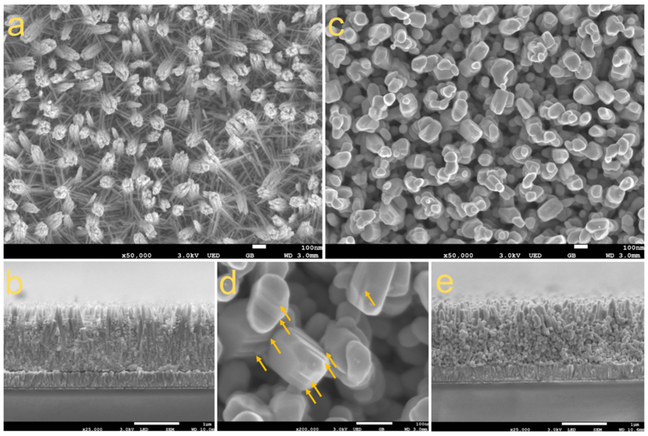

**Figure 8.** SEM images of (a and b) the 350 °C annealed film and (c−e) the 550 °C annealed film.

Before the optical properties were investigated by the relative instruments, the films were observed visually. The inset digital photograph of Figure 9 indicates that the films present distinct color changes. The blue faded and a fine yellow appeared as the annealing temperature rose. However, the unannealed film and the 350 °C annealed film exhibited good transparent properties. The UV−vis−NIR spectra were used to provide further insight into the optical properties of the films. Figure 9 displays the transmittance and reflectance spectra of the films. From the transmittance spectra, it can be seen that the branched

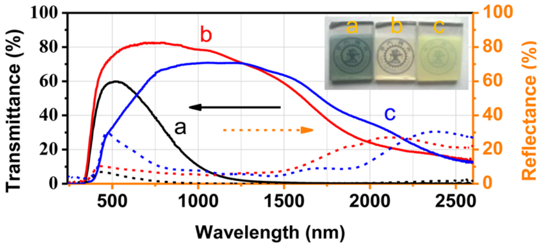

**Figure 9.** Optical images of (a) the branched $(NH_4)_xWO_3$ nanowire array film, (b) the 350 °C annealed film, and (c) the 550 °C annealed film.

$(NH_4)_xWO_3$ nanowire array film exhibited a relatively low NIR transmittance (lower than 20% in 900−1250 nm and almost 0% in 1250−2600 nm) but a considerable luminous transmittance (60%). This phenomenon indicates that the as-prepared branched $(NH_4)_xWO_3$ nanowire array film can be used as a NIR shielder.

After annealing at 350 °C, both the transmittance and reflectance in the vis−NIR range obviously increase. The above analysis suggests that the main changes were the reduction of $W^{5+}$ (oxygen deficiency) and $NH_4^+$. Although oxygen deficiency was considered to be very important in NIR absorption of the $WO_{3-x}$ films, the effect of $NH_4^+$ cannot be ruled out because of the absorption band of $NH_4^+$ in IR light.[44−48] Thus, the different performances of the unannealed film and the 350 °C annealed film in the vis−NIR range absorption should be due to the joint influence of both $NH_4^+$ and $W^{5+}$.[16]

The fine yellow color and the porous nanorod array structure of the 550 °C annealed film indicated that the as-prepared monoclinic $WO_3$ film may have pretty good PEC properties. The photocurrent density performance of the films was tested under a simulated light source, as shown in Figure 10. Before annealing, the branched $(NH_4)_xWO_3$ nanowire array film exhibited a weak response to light illumination. After annealing at 350 °C, although an obvious photoelectric response appeared, the photocurrent density was still quite low. However, the 550 °C annealed film showed a pretty good photoelectric response. The photocurrent density could reach 1.05 mA/cm$^2$ at an applied potential of 1.1 V versus SCE, which is comparable with the reported $WO_3$ photoanodes.[33−39] However, different light sources, electrolytes, and counter electrodes can influence the current−potential performance of the films.[36] For the purposes of comparison and practical applications, the global standard spectrum (AM1.5) is commonly used as the light source in research. Despite $Na_2SO_4$ (neutral, used in this work), some acidic or alkaline solution is also often used as the electrolyte. For $WO_3$-based photoelectrodes, the commonly used electrolytes are $Na_2SO_4$ (neutral)[33,34,38] and $H_2SO_4$ (acidic)[35,37,39] solutions, while $WO_3$ is more likely to encounter photocorrosion in a neutral electrolyte than in an acidic electrolyte. Additionally, the photostability test on the porous $WO_3$ nanorod array film is displayed in Figure S5 in the SI.

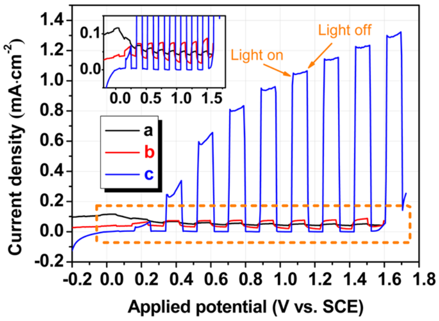

**Figure 10.** Current−potential curves of (a) the branched $(NH_4)_xWO_3$ nanowire array film, (b) the 350 °C annealed film, and (c) the 550 °C annealed film.

## CONCLUSIONS

In summary, the branched $(NH_4)_xWO_3$ nanowire array film was successfully fabricated via a facile one-step hydrothermal treatment. The chemical composition of the as-prepared blue film was determined by XPS and XRD. As the annealing temperature increased, $NH_4^+$ and $W^{5+}$ gradually faded away from the film, and the hexagonal $(NH_4)_xWO_3$ transformed to monoclinic $WO_3$. The SEM and TEM images display the $(NH_4)_xWO_3$ film has a 3D branched nanostructure, and the $WO_3$ film has a porous nanorod array structure. Combination analysis of HRTEM and XRD shows that both trunks and branches of the branched nanowire array preferred to grow along the *c* axis. Moreover, on the basis of the results of an optical and PEC test, the branched $(NH_4)_xWO_3$ nanowire array film exhibits fine NIR shield properties and can be used as a NIR shielder, while the porous $WO_3$ nanorod array film has pretty good PEC properties and can be used for water splitting.

## ASSOCIATED CONTENT

### Ⓢ Supporting Information

SEM images for the films with different preparation conditions, XRD patterns and high-resolution XPS spectra of 250 and 450 °C annealed films, current−time curves of the porous $WO_3$ nanorod array film, and optical images and PEC performance of the branched $(NH_4)_xWO_3$ nanowire array film before and after 2 months of exposure in the atmosphere. This material is available free of charge via the Internet at http://pubs.acs.org.

## AUTHOR INFORMATION

### Corresponding Author

*E-mail: mingtao@mail.xjtu.edu.cn. Tel: (+86) 29-8266-8296. Fax: (+86) 29-8266-9033.

### Notes

The authors declare no competing financial interest.

## ACKNOWLEDGMENTS

We are grateful for financial support from the National Natural Science Foundation of China (Grants 51121092, 51302211, and 51323011), and M.L. acknowledges financial support from the Shaanxi Provincial Natural Science Foundation (Grant 2012JQ7033) and the Specialized Research Fund for the Doctoral Program of Higher Education (Grant 20120201120057).

## REFERENCES

(1) Cheng, C.; Fan, H. J. Branched Nanowires: Synthesis and Energy Applications. *Nano Today* **2012**, *7*, 327−343.

(2) Bierman, M. J.; Jin, S. Potential Applications of Hierarchical Branching Nanowires in Solar Energy Conversion. *Energy Environ. Sci.* **2009**, *2*, 1050−1059.

(3) Yella, A.; Lee, H. W.; Tsao, H. N.; Yi, C. Y.; Chandiran, A. K. Porphyrin-Sensitized Solar Cells with Cobalt(II/III)-Based Redox Electrolyte Exceed 12% Efficiency. *Science* **2011**, *334*, 1203−1203.

(4) Liu, R.; Duay, J.; Lee, S. B. Heterogeneous Nanostructured Electrode Materials for Electrochemical Energy Storage. *Chem. Commun.* **2011**, *47*, 1384−1404.

(5) Cho, I. S.; Chen, Z.; Forman, A. J.; Kim, D. R.; Rao, P. M.; Jaramillo, T. F.; Zheng, X. Branched $TiO_2$ Nanorods for Photoelectrochemical Hydrogen Production. *Nano Lett.* **2011**, *11*, 4978−4984.

(6) Zhou, W.; Cheng, C.; Liu, J.; Tay, Y. Y.; Jiang, J.; Jia, X.; Zhang, J.; Gong, H.; Hng, H. H.; Yu, T.; Fan, H. J. Epitaxial Growth of Branched $\alpha$-$Fe_2O_3/SnO_2$ Nano-Heterostructures with Improved Lithium-Ion Battery Performance. *Adv. Funct. Mater.* **2011**, *21*, 2439−2445.

(7) Mai, L.-Q.; Yang, F.; Zhao, Y.-L.; Xu, X.; Xu, L.; Luo, Y.-Z. Hierarchical $MnMoO_4/CoMoO_4$ Heterostructured Nanowires with Enhanced Supercapacitor Performance. *Nat. Commun.* **2011**, *2*, 381.

(8) Zhou, S.; Liu, X.; Wang, D. Si/$TiSi_2$ Heteronanostructures as High-Capacity Anode Material for Li Ion Batteries. *Nano Lett.* **2010**, *10*, 860−863.

(9) Jiang, X. C.; Tian, B. Z.; Xiang, J.; Qian, F.; Zheng, G. F.; Wang, H. T.; Mai, L. Q.; Lieber, C. M. Rational Growth of Branched Nanowire Heterostructures with Synthetically Encoded Properties and Function. *Proc. Natl. Acad. Sci. U.S.A.* **2011**, *108*, 12212−12216.

(10) Jung, H. Y.; Karimi, M. B.; Hahm, M. G.; Ajayan, P. M.; Jung, Y. J. Transparent, Flexible Supercapacitors from Nano-Engineered Carbon Films. *Sci. Rep.* **2012**, *2*, 773.

(11) Guo, K.; Liu, Z.; Zhou, C.; Han, J.; Zhao, Y.; Liu, Z.; Li, Y.; Cui, T.; Wang, B.; Zhang, J. Fabrication of $TiO_2$ Nano-Branched Arrays/$Cu_2S$ Composite Structure and Its Photoelectric Performance. *Appl. Catal., B* **2014**, *154−155*, 27−35.

(12) Wang, H.; Bai, Y.; Wu, Q.; Zhou, W.; Zhang, H.; Li, J.; Guo, L. Rutile $TiO_2$ Nano-Branched Arrays on FTO for Dye-Sensitized Solar Cells. *Phys. Chem. Chem. Phys.* **2011**, *13*, 7008−7013.

(13) Kargar, A.; Sun, K.; Jing, Y.; Choi, C.; Jeong, H.; Jung, G. Y.; Jin, S.; Wang, D. 3D Branched Nanowire Photoelectrochemical Electrodes for Efficient Solar Water Splitting. *ACS Nano* **2013**, *7*, 9407−9415.

(14) Kargar, A.; Jing, Y.; Kim, S. J.; Riley, C. T.; Pan, X.; Wang, D. ZnO/CuO Heterojunction Branched Nanowires for Photoelectrochemical Hydrogen Generation. *ACS Nano* **2013**, *7*, 11112−11120.

(15) Guo, C.; Yin, S.; Dong, Q.; Sato, T. Simple Route to $(NH_4)_XWO_3$ Nanorods for Near Infrared Absorption. *Nanoscale* **2012**, *4*, 3394−3398.

(16) Kang, L.; Xu, W.; Wang, K.; Liang, W.; Liu, X.; Gao, F.; Lan, A.; Yang, Y.; Gao, Y. Transparent $(NH_4)_XWO_3$ Colloidal Dispersion and Solar Control Foils: Low Temperature Synthesis, Oxygen Deficiency Regulation and NIR Shielding Ability. *Sol. Energy Mater. Sol. Cells* **2014**, *128*, 184−189.

(17) Guo, C.; Yin, S.; Zhang, P.; Yan, M.; Adachi, K.; Chonan, T.; Sato, T. Novel Synthesis of Homogenous $Cs_xWO_3$ Nanorods with Excellent NIR Shielding Properties by a Water Controlled-Release Solvothermal Process. *J. Mater. Chem.* **2010**, *20*, 8227−8229.

(18) Guo, C.; Yin, S.; Yan, M.; Sato, T. Facile Synthesis of Homogeneous $Cs_xWO_3$ Nanorods with Excellent Low-Emissivity and NIR Shielding Property by a Water Controlled-Release Process. *J. Mater. Chem.* **2011**, *21*, 5099−5105.

(19) Guo, C.; Yin, S.; Huang, L.; Sato, T. Synthesis of One-Dimensional Potassium Tungsten Bronze with Excellent Near-Infrared Absorption Property. *ACS Appl. Mater. Interfaces* **2011**, *3*, 2794−2799.

(20) Guo, C.; Yin, S.; Huang, L.; Yang, L.; Sato, T. Discovery of an Excellent IR Absorbent with a Broad Working Waveband: $Cs_xWO_3$ Nanorods. *Chem. Commun.* **2011**, *47*, 8853−8855.

(21) Li, X. P.; Xiang, X. D.; Yang, H. Y.; Wang, X. J.; Tan, C. L.; Li, W. S. Hydrogen Tungsten Bronze-Supported Platinum as Electrocatalyst for Methanol Oxidation. *Fuel Cells* **2013**, *13*, 314−318.

(22) Yoon, D.; Manthiram, A. Hydrogen Tungsten Bronze as a Decoking Agent for Long-Life, Natural Gas-Fueled Solid Oxide Fuel Cells. *Energy Environ. Sci.* **2014**, *7*, 3069−3076.

(23) Szilágyi, I. M.; Madarász, J.; Pokol, G.; Király, P.; Tárkányi, G.; Saukko, S.; Mizsei, J.; Tóth, A. L.; Szabó, A.; Varga-Josepovits, K. Stability and Controlled Composition of Hexagonal $WO_3$. *Chem. Mater.* **2008**, *20*, 4116−4125.

(24) Hill, J. C.; Choi, K.-S. Effect of Electrolytes on the Selectivity and Stability of N-type $WO_3$ Photoelectrodes for Use in Solar Water Oxidation. *J. Phys. Chem. C* **2012**, *116*, 7612−7620.

(25) Kalanur, S. S.; Hwang, Y. J.; Chae, S. Y.; Joo, O. S. Facile Growth of Aligned $WO_3$ Nanorods on FTO Substrate for Enhanced Photoanodic Water Oxidation Activity. *J. Mater. Chem. A* **2013**, *1*, 3479−3488.

(26) Lee, S. H.; Deshpande, R.; Parilla, P. A.; Jones, K. M.; To, B.; Mahan, A. H.; Dillon, A. C. Crystalline $WO_3$ Nanoparticles for Highly Improved Electrochromic Applications. *Adv. Mater.* **2006**, *18*, 763−766.

(27) Bechinger, C.; Ferrere, S.; Zaban, A.; Sprague, J.; Gregg, B. A. Photoelectrochromic Windows and Displays. *Nature* **1996**, *383*, 608−610.

(28) Gratzel, M. Materials science: Ultrafast Colour Displays. *Nature* **2001**, *409*, 575−576.

(29) Bignozzi, C. A.; Caramori, S.; Cristino, V.; Argazzi, R.; Meda, L.; Tacca, A. Nanostructured Photoelectrodes Based on $WO_3$: Applications to Photooxidation of Aqueous Electrolytes. *Chem. Soc. Rev.* **2013**, *42*, 2228−2246.

(30) Solarska, R.; Królikowska, A.; Augustyński, J. Silver Nanoparticle Induced Photocurrent Enhancement at $WO_3$ Photoanodes. *Angew. Chem., Int. Ed.* **2010**, *49*, 7980−7983.

(31) Solarska, R.; Alexander, B.; Augustynski, J. Electrochromic and Structural Characteristics of Mesoporous $WO_3$ Films Prepared by a Sol−Gel Method. *J. Solid State Electrochem.* **2004**, *8*, 748−756.

(32) Santato, C.; Ulmann, M.; Augustynski, J. Photoelectrochemical Properties of Nanostructured Tungsten Trioxide Films. *J. Phys. Chem. B* **2001**, *105*, 936−940.

(33) Su, J.; Feng, X.; Sloppy, J. D.; Guo, L.; Grimes, C. A. Vertically Aligned $WO_3$ Nanowire Arrays Grown Directly on Transparent Conducting Oxide Coated Glass: Synthesis and Photoelectrochemical Properties. *Nano Lett.* **2010**, *11*, 203−208.

(34) Qin, D.-D.; Tao, C.-L.; Friesen, S. A.; Wang, T.-H.; Varghese, O. K.; Bao, N.-Z.; Yang, Z.-Y.; Mallouk, T. E.; Grimes, C. A. Dense Layers of Vertically Oriented $WO_3$ Crystals as Anodes for Photoelectrochemical Water Oxidation. *Chem. Commun.* **2012**, *48*, 729−731.

(35) Spurgeon, J. M.; Velazquez, J. M.; McDowell, M. T. Improving $O_2$ Production of $WO_3$ Photoanodes with $IrO_2$ in Acidic Aqueous Electrolyte. *Phys. Chem. Chem. Phys.* **2014**, *16*, 3623−3631.

(36) Solarska, R.; Jurczakowski, R.; Augustynski, J. A Highly Stable, Efficient Visible-Light Driven Water Photoelectrolysis System Using a Nanocrystalline $WO_3$ Photoanode and a Methane Sulfonic Acid Electrolyte. *Nanoscale* **2012**, *4*, 1553−1556.

(37) Królikowska, A.; Barczuk, P.; Jurczakowski, R.; Augustynski, J. The Core−Shell Nature of Nanostructured $WO_3$ Photoelectrodes Demonstrated in Spectroelectrochemical Studies. *J. Electroanal. Chem.* **2011**, *662*, 229−239.

(38) Barczuk, P. J.; Krolikowska, A.; Lewera, A.; Miecznikowski, K.; Solarska, R.; Augustynski, J. Structural and Photoelectrochemical Investigation of Boron-Modified Nanostructured Tungsten Trioxide Films. *Electrochim. Acta* **2013**, *104*, 282−288.

(39) Hilaire, S.; Suess, M. J.; Kranzlin, N.; Bienkowski, K.; Solarska, R.; Augustynski, J.; Niederberger, M. Microwave-Assisted Nonaqueous Synthesis of $WO_3$ Nanoparticles for Crystallographically Oriented Photoanodes for Water Splitting. *J. Mater. Chem. A* **2014**, *2*, 20530−20537.

(40) Gu, Z.; Ma, Y.; Zhai, T.; Gao, B.; Yang, W.; Yao, J. A Simple Hydrothermal Method for the Large-Scale Synthesis of Single-Crystal Potassium Tungsten Bronze Nanowires. *Chem.—Eur. J.* **2006**, *12*, 7717−7723.

(41) Griffith, C. S.; Luca, V. Ion-Exchange Properties of Microporous Tungstates. *Chem. Mater.* **2004**, *16*, 4992−4999.

(42) Chen, F.; Zhou, R.; Yang, L.; Shi, M.; Wu, G.; Wang, M.; Chen, H. One-Step Fabrication of CdS Nanorod Arrays via Solution Chemistry. *J. Phys. Chem. C* **2008**, *112*, 13457−13462.

(43) Liu, Y.; Jiang, J.; Xu, Q.; Li, M.; Guo, L. Photoelectrochemical Performance of CdS Nanorods Grafted Vertically Aligned $TiO_2$ Nanorods. *Mater. Res. Bull.* **2013**, *48*, 4548−4554.

(44) Busigny, V.; Cartigny, P.; Philippot, P.; Javoy, M. Ammonium Quantification in Muscovite by Infrared Spectroscopy. *Chem. Geol.* **2003**, *198*, 21−31.

(45) Guo, C.; Yin, S.; Yan, M.; Kobayashi, M.; Kakihana, M.; Sato, T. Morphology-Controlled Synthesis of $W_{18}O_{49}$ Nanostructures and Their Near-Infrared Absorption Properties. *Inorg. Chem.* **2012**, *51*, 4763−4771.

(46) Mo, Y.-G.; Dillon, R.; Snyder, P. Visible and Infrared Photochromic Properties of Amorphous $WO_{3-x}$ films. *J. Vac. Sci. Technol. A* **1999**, *17*, 2933−2938.

(47) Lu, Y.; Qiu, H. Laser Coloration and Bleaching of Amorphous $WO_3$ Thin Film. *J. Appl. Phys.* **2000**, *88*, 1082−1087.

(48) Busigny, V.; Cartigny, P.; Philippot, P.; Javoy, M. Quantitative Analysis of Ammonium in Biotite Using Infrared Spectroscopy. *Am. Mineral.* **2004**, *89*, 1625−1630.